

Flow of truncated power-law fluid in fracture channels of variable aperture

G. Felisa^a, A. Lenci^a, I. Lauriola^a, S. Longo^b, V. Di Federico^a

^a*Dipartimento di Ingegneria Civile, Chimica, Ambientale e dei Materiali (DICAM),
Università di Bologna, Viale Risorgimento, 2, 40136 Bologna, Italy*

^b*Dipartimento di Ingegneria e Architettura (DIA), Università di Parma, Parco Area
delle Scienze, 181/A, 43124 Parma, Italy*

Abstract

A conceptual model is presented for non-Newtonian fluid flow in a rough channel representing a single fracture. The fluid rheology is described via a truncated power-law (TPL) model approximating the Carreau constitutive equation, while the aperture variation along the channel is modeled via a stochastic distribution of assigned mean and variance; the lognormal and gamma distributions are considered, together with a deterministic variation of sinusoidal behavior. The flowrate in a fracture subject to an external pressure gradient is derived under the lubrication approximation for the two limiting cases of a pressure gradient which is i) perpendicular and ii) parallel to aperture variation; these parallel and serial arrangements (PA or SA) provide an upper and lower bound to the fracture conductance. Different combinations of the parameters describing the fluid rheology and the variability of the aperture field are considered for a sensitivity analysis. Results are also compared with those valid for a pure power-law (PL) fluid which provides a relevant benchmark. The channel flowrate shows a direct/inverse dependency upon aperture variability for PA/SA. The difference in flowrate between the PL and TPL models is positively affected by aperture variability and pressure gradient, negatively affected by flow behaviour index, while its sign is positive or negative depending on PA/SA. The influence of the specific pdf adopted for the aperture field is moderate, an increasing function of aperture variability and depends on the third and fourth moment of the distribution. The conductance for a deterministic aperture variation exhibits the same trends as a stochastic variation, with differences from the latter depending on aperture variability and flow arrangement.

Keywords: fracture, non-Newtonian, truncated power-law, aperture variation, lubrication theory

1. Introduction

Hydraulic fracturing is largely used for optimal exploitation of oil, gas and thermal reservoirs. Non-Newtonian fluids are most frequently used in this type of operations [1, 2]; the challenge of modeling flow of these rheologically complex fluids is compounded by the possible interaction of multiple non-Newtonian fluids [3]. Complex fluids interact with pre-existing rock fractures also during drilling operations [4, 5], enhanced oil recovery [6], and environmental remediation, and other natural phenomena such as magma intrusions, sand intrusions, and mud volcanoes (see Medina *et al.*, 2015 [7] and references therein). Hence, it is important to model non-Newtonian flow in fractured media. A first step in this process is a detailed understanding of flow in a single fracture, as the space between fracture walls (termed fracture aperture) is typically spatially variable [8].

A large bibliography exists on Newtonian flow in single, variable aperture fractures. Neuzil and Tracy [9] and Tsang [10] adopted a one-dimensional channel model, with channels described by an aperture density distribution and a spatial correlation length. Other authors [11, 12, 13, 14] extended the model to two-dimensional spatial variability of assigned correlation function, while other studies [15, 16, 17, 18] simulated the fracture surface roughness using fractal models of surface topography. Comprehensive reviews on flow in a single fracture were provided in [19, 20, 21, 22].

Ultimately, stochastic modeling of aperture variability at the single fracture scale leads to determination of the flowrate under a given pressure gradient as a function of the parameters describing the variability of the aperture field and the fluid rheological behaviour. From the flowrate, a flow, or hydraulic aperture can then be derived [23]; a second equivalent aperture can be defined for transport, and usually differs from the hydraulic aperture [24].

The equivalent flow aperture for flow of non-Newtonian fluids of power-law nature in single, variable aperture fractures has been obtained with an heuristic approach by Di Federico for a stochastic variation of assigned distribution [25] and for deterministic variations [26, 27]. Detailed numerical modeling of flow of a power-law fluid in a variable aperture fracture was performed by Lavrov [28, 29], whose work demonstrated that pronounced

channelization effects are associated to a nonlinear fluid rheology; a further study by Lavrov [30] validated the simplified model of [26]. The availability of an equivalent flow aperture as a function of the parameters describing the fluid rheology and the aperture variability is enticing, as it allows taking their interaction into account when modeling flow in fracture networks at a larger scale [31]. Bingham fluid flow in a variable aperture channel was studied analytically and numerically by Roustaei *et al.* [32], highlighting the progressive departure from the lubrication approximation with increasing heterogeneity, the onset of fouling layers, and the existence of a limiting pressure gradient.

Another relevant issue in non-Newtonian fracture flow is the rheological nature of the fluid. The constitutive model routinely used for hydrofracturing modeling is the simple, two-parameter power-law [33]. Yet this model does not characterize real fluids at low and high shear rates, as it implies, for shear-thinning fluids, an apparent viscosity which becomes unbounded for zero shear rate and tends to zero for infinite shear rate. On the contrary, the four-parameter Carreau constitutive equation includes asymptotic values of the apparent viscosity at those limits. Lavrov [34] showed the Carreau rheological equation is well approximated by the truncated power-law model, and suggested to adopt the latter model for numerical modeling of flow in variable aperture fractures. To this end, he derived the expressions for flow of a truncated power-law fluid between parallel walls under a constant pressure gradient. A method to predict the flow of yield stress fluids described by a Herschel-Bulkley model and of shear thinning fluids without yield stress described by Carreau model through rough fractures was recently proposed and experimentally validated [35, 36].

This paper extends the adoption of the truncated power-law model to fractures of variable aperture, in a stochastic or deterministic fashion, with the aim of understanding the joint influence of rheology and aperture spatial variability in a simplified geometrical setup where the variability is confined to one-direction, looking at the two limit cases where the aperture variability is either parallel or perpendicular to the flow direction. This assumption, which admittedly simplifies the real flow field, aims at providing reference benchmarks to be compared with more complex simulations. Section 2 summarizes results on flow of a truncated power-law fluid between parallel walls; Section 3 presents the general expressions of the flowrate for flow perpendicular and parallel to aperture variation; Section 4 deals with a stochastic aperture variation, and illustrates results stemming from the adoption of two

different pdfs for the aperture distribution (lognormal and gamma). Section 6 applies the same simplified methodology to a deterministic aperture variation of sinusoidal behaviour. Then results obtained for the truncated model are compared with those earlier obtained for pure power-law fluids. Section 7 reports some conclusions.

2. Flow of truncated power-law fluid flow in a constant aperture fracture

Consider the flow of a shear-thinning non-Newtonian fluid in a fracture of length L , width W and constant aperture b ; the coordinate system is shown in Figures 1(a)-(b); the fracture walls are at $z = +b/2$ and $z = -b/2$. Suppose a uniform, positive pressure gradient $p_x = [p(0) - p(L)]/L$ is applied in the x direction. Assuming that $b \ll W$, the velocity components in the y and z directions are zero, and the only nonzero velocity component, v_x , is solely a function of z . The fluid is described by the rheological truncated power-law model, reading, in the simple shear situation described above, $\tau = \mu_a \dot{\gamma}$, with τ shear stress, and $\dot{\gamma}$ shear rate. The apparent viscosity μ_a is given by

$$\begin{aligned} \mu_a &= \mu_0 & \text{for } \dot{\gamma} \leq \dot{\gamma}_1; \\ \mu_a &= m\dot{\gamma}^{n-1} & \text{for } \dot{\gamma}_1 < \dot{\gamma} < \dot{\gamma}_2; \\ \mu_a &= \mu_\infty & \text{for } \dot{\gamma} \geq \dot{\gamma}_2; \end{aligned} \quad (1)$$

In Eq.(1), depicted in Figure 1c, μ_0 is the viscosity at zero shear rate, μ_∞ is the limiting viscosity for $\dot{\gamma} \rightarrow \infty$, n and m are the rheological and consistency index, respectively, $\dot{\gamma}_1 = (m/\mu_0)^{1/(1-n)}$ is the lower shear rate at which the high viscosity cutoff μ_0 is introduced, and $\dot{\gamma}_2 = (m/\mu_\infty)^{1/(1-n)}$ is the higher shear rate at which the low viscosity cutoff μ_∞ is introduced. The above four-parameter model is identical to the pure power-law model of parameters n and m in the intermediate shear stress range $\dot{\gamma}_1 < \dot{\gamma} < \dot{\gamma}_2$, and overcomes the limitation of having $\mu_a \rightarrow \infty$ for $\dot{\gamma} \rightarrow 0$ and $\mu_a \rightarrow 0$ for $\dot{\gamma} \rightarrow \infty$. Lavrov [34] showed that the truncated power-law model is practically indistinguishable, for practical purposes, from the Carreau model. He also derived the velocity field $v_x(z)$ and the flowrate per unit width $q_x = Q_x/W$ under a constant pressure gradient p_x . Depending on the aperture value, the flowrate can take three different expressions, namely

$$q_{xI}(b) = \frac{b^3 p_x}{12\mu_0} \quad \text{for } b < b_1 = \frac{2\mu_0 \dot{\gamma}_1}{p_x}; \quad (2a)$$

$$q_{xII}(b) = \frac{2(1-n)m^{3/(1-n)}}{3(2n+1)\mu_0^{(2n+1)/(1-n)}p_x^2} + \frac{nb^{(2n+1)/n}}{2n+1} \left(\frac{p_x}{2^{n+1}m} \right)^{1/n} \quad (2b)$$

for $b_1 < b < b_2$;

$$q_{xIII}(b) = \frac{b^3 p_x}{12\mu_\infty} - \frac{2(1-n)m^{3/(1-n)}}{3(2n+1)p_x^2} \left(\frac{1}{\mu_\infty^{(2n+1)/(1-n)}} - \frac{1}{\mu_0^{(2n+1)/(1-n)}} \right) \quad (2c)$$

for $b > b_2 = \frac{2m\dot{\gamma}_2^n}{p_x}$;

According to Eqs. (2a)-(2b)-(2c), three flow regimes (I = low shear rate regime, II = intermediate shear rate regime, and III = high shear rate regime) are possible within the fracture, depending on the relationship between its aperture b and the two threshold apertures b_1 and b_2 .

3. Flow in a variable aperture channel

In single fracture flow modeling, the fracture aperture $b(x, y)$ is usually taken to vary as a two-dimensional, spatially homogeneous and correlated random field, characterized by a probability density function $f(b)$ of given mean $\langle b \rangle$ and variance σ_b^2 , and possibly spatial correlation described by an aperture autocovariance function of given integral scale I or integral scales I_x and I_y in the anisotropic case (alternatively a fractal distribution of given Hurst coefficient H and correlated at all scales is adopted).

If an anisotropic aperture field of anisotropy ratio $e = I_y/I_x$ is considered, the two limiting cases $e = 0$ and $e = \infty$ give rise to a purely one-dimensional aperture variation; consequently, flow under an external pressure gradient can be considered to take place either transverse (case 1, Figure 2a) or parallel to aperture variability (case 2, Figure 2b). This approach was used for Newtonian flow by Silliman [23] to infer estimates of 2-D hydraulic and transport apertures, by Zimmerman [37] to determine the hydraulic aperture under deterministic sinusoidal variations, and by Di Federico [26, 25] to derive estimates of hydraulic aperture for non-Newtonian power-law flow under both deterministic and stochastic aperture variations, respectively. Lavrov [30] validated the approach with two-dimensional numerical simulations conducted for a deterministic, sinusoidal aperture profile in both directions. Comparison of his results with the geometric average of flowrates for one-dimensional sinusoidal variations only along and only across the flow (cases 1 and 2 respectively but with a sinusoidal variation, see Section 5) showed a

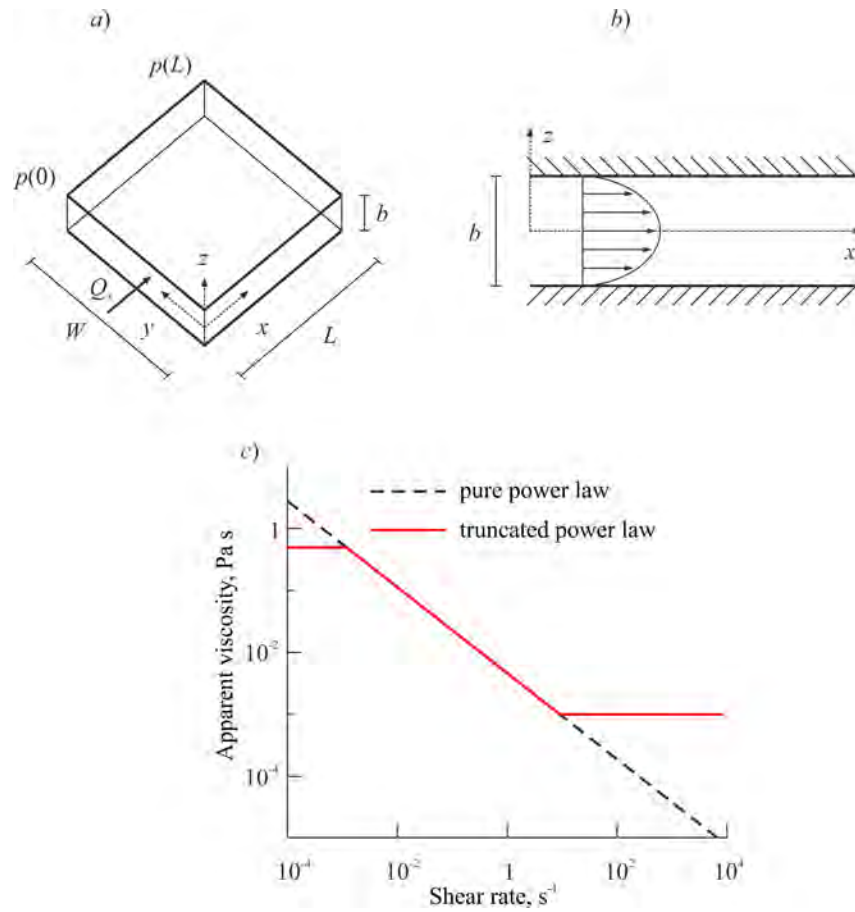


Figure 1: Configuration of the fractures and rheological approximation. *a*) Fracture sketch with applied pressure gradient; *b*) fracture profile in the x direction; *c*) apparent viscosity μ_a as a function of shear rate for the two models: truncated and pure power-law, respectively.

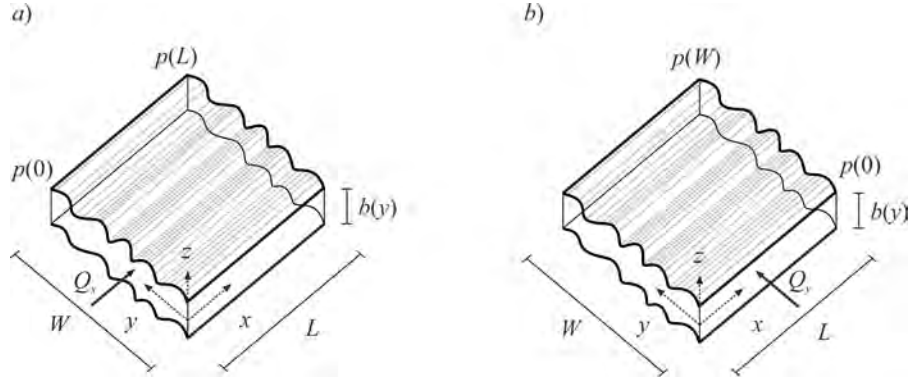


Figure 2: Configuration of the fracture. *a)* Case 1: flow perpendicular to aperture variation described by the aperture density function $f(b)$; *b)* case 2: flow parallel to aperture variation described by the aperture density function $f(b)$.

relative discrepancy in terms of equivalent aperture equal to less than 10% for $\delta < 0.4$, δ being the non-dimensional amplitude of the aperture variation. In the sequel, we consider first case 1, then case 2.

3.1. Flow parallel to constant aperture channels

Consider a fracture of dimensions L and W in the x and y direction, respectively, and aperture varying only in the y direction. Consider flow in the direction x parallel to constant aperture channels, i.e., transverse to aperture variation (case 1, Figure 2a); the applied pressure gradient is $p_x = [p(0) - p(L)]/L$; the volumetric flux is obtained through the following procedure. The fracture model is discretized into N neighboring parallel channels, each having equal width $\Delta y = W/N$, length L and constant aperture b_i . Depending on the local aperture value, in each channel the flow regime is either I, or II, or III, and the corresponding flowrate per unit width is given either by (2a), (2b), or (2c). The number of channels in each regime is N_I , N_{II} , N_{III} , respectively, and the total width of the channels in each regime is W_I , W_{II} , W_{III} with $N = N_I + N_{II} + N_{III}$ and $W = W_I + W_{II} + W_{III}$; the i -th channel in each regime j ($j = I, II, III$) has width $W_{ji} = W_j/N_j$. Assuming that the shear between neighboring channels and the drag against the connecting walls may be neglected, the total flowrate in the x direction

is

$$Q_x = \sum_{i=1}^{N_I} q_I(b_i)W_{Ii} + \sum_{i=1}^{N_{II}} q_{II}(b_i)W_{IIi} + \sum_{i=1}^{N_{III}} q_{III}(b_i)W_{IIIi}. \quad (3)$$

This assumption is acceptable for channels with a smooth variation of the aperture, i.e. with a smooth variation of the flowrate along the y direction, otherwise a linear momentum sharing between the neighbouring channels due to tangential stress in the $x - z$ plane is expected. Taking the limit as $N_j \rightarrow \infty$, the width of each channel tends to zero and the discrete aperture variation to a continuous one; then under ergodicity, and exploiting the previous relationships, (3) gives for the flowrate per unit width in the x direction the expression

$$q_x = \frac{Q_x}{W} = I_I \frac{p_x}{12\mu_0} + \left[P_{II} \frac{2(1-n)m^{3/(1-n)}}{3(2n+1)\mu_0^{(2n+1)/(1-n)} p_x^2} + \frac{n}{2n+1} I_{II} \left(\frac{p_x}{2^{n+1}m} \right)^{1/n} \right] + \left[I_{III} \frac{p_x}{12\mu_\infty} - P_{III} \frac{2(1-n)m^{3/(1-n)}}{3(2n+1)p_x^2} \left(\frac{1}{\mu_\infty^{(2n+1)/(1-n)}} - \frac{1}{\mu_0^{(2n+1)/(1-n)}} \right) \right], \quad (4)$$

where

$$I_I = \int_0^{b_1} b^3 f(b) db; \quad I_{II} = \int_{b_1}^{b_2} b^{(2n+1)/n} f(b) db; \quad I_{III} = \int_{b_2}^{\infty} b^3 f(b) db; \quad (5)$$

$$P_{II} = F(b_2) - F(b_1); \quad P_{III} = 1 - F(b_2), \quad (6)$$

in which $f(b)$ and $F(b)$ are the pdf and cumulative distribution function of the aperture field, respectively.

3.2. Flow perpendicular to constant aperture channels

Consider now flow in the y direction perpendicular to constant aperture channels, i.e. parallel to aperture variation (case 2, Figure 2b); the fracture length is W and the applied pressure gradient is $p_y = [p(0) - p(W)]/W$, while L is the fracture width perpendicular to gradient. Discretizing the fracture model into N cells of equal length $\Delta y = W/N$ in series, each cell has width L and constant aperture b_i . By virtue of mass conservation, volumetric flux Q_y through each cell is the same; depending on the local aperture value, in each channel the flow regime is either I, or II, or III, and the corresponding flowrate per unit width $q_y = Q_y/L$ is given, respectively, by the counterparts

of Eqs. (2a), (2b), or (2c) upon substitution of the subscript x with the subscript y ; this is so neglecting the pressure losses due to the succession of constrictions and enlargements. The number of cells in each regime is N_I , N_{II} , N_{III} , respectively, and the total length of the cells in each regime is W_I , W_{II} , W_{III} , with $N = N_I + N_{II} + N_{III}$ and $W = W_I + W_{II} + W_{III}$; the i -th cell in each regime j ($j = I, II, III$) has length $W_{ji} = W_j/N_j$. The total pressure loss along the fracture, Δp_y , can be expressed as the sum of pressure losses in each cell, Δp_{yi} , as $\Delta p_y = [p(0) - p(W)] = \sum_{i=1}^N \Delta p_{yi}$. This in turn yields the mean pressure gradient p_y as

$$p_y = \sum_{i=1}^{N_I} p_{yIi} \frac{W_{Ii}}{W} + \sum_{i=1}^{N_{II}} p_{yIIi} \frac{W_{IIi}}{W} + \sum_{i=1}^{N_{III}} p_{yIIIi} \frac{W_{IIIi}}{W}, \quad (7)$$

where p_{yji} is the pressure gradient in the i -th cell under flow regime j ($j = I, II, III$). Taking the limit as $N_j \rightarrow \infty$, the length of each cell tends to zero and the discrete aperture variation to a continuous one; then under ergodicity, and exploiting the previous relationships, Equation (7) gives for the mean pressure gradient in the y direction the expression

$$p_y = \int_0^{b_1} p_{yI} f(b) db + \int_{b_1}^{b_2} p_{yII} f(b) db + \int_{b_2}^{\infty} p_{yIII} f(b) db, \quad (8)$$

where the pressure gradient for each infinitesimal cell of constant aperture, i.e. $p_{yj} = p_{yj}(q_y, f(b), b_1, b_2, \mu_0, m, n, \mu_\infty)$, can be expressed as a function of the unknown flowrate per unit width $q_{yI} = q_{yII} = q_{yIII} = q_y$, and the parameters describing the fracture geometry and the fluid rheology, upon inverting Equations (2a), (2b), or (2c), written replacing the subscript x with the subscript y . This allows deriving, albeit numerically, the flowrate per unit width as a function of the applied pressure gradient and problem parameters as done in (4) for channels in parallel. An alternative formulation of the problem, using the same formalism adopted for flow parallel to constant aperture channel, is presented in Appendix A and leads to the same results.

4. Estimate of flowrate and discussion

Different distributions are adopted for the aperture field, consistently with earlier work on flow and transport in variable aperture fractures [12, 13]. In the following, i) lognormal, and ii) gamma distribution are considered, the latter covering for values of the parameter $d > 3 - 4$ also the normal case.

4.1. Lognormal distribution

Lognormal distributions for the aperture field were adopted by [12] and [13]. Its probability distribution function is given by

$$f(b) = \frac{1}{b\sigma\sqrt{2\pi}} \exp \left[-\frac{(\ln b - \ln b_g)^2}{2\sigma^2} \right], \quad (9)$$

where $b_g = \langle b \rangle \exp(-\sigma^2/2)$ is the geometric mean, $\langle b \rangle$ the arithmetic mean, and σ^2 the variance of $\ln b$. Utilizing Eqs. (4)-(5) with Equation (6) gives for the factors $I_j (j = I, II, III)$ and $P_j (j = II, III)$ the following expressions:

$$\begin{aligned} I_I &= \frac{\langle b \rangle^3}{2} \exp(3\sigma^2) \left[1 + \operatorname{erf} \left(\frac{1}{\sqrt{2}\sigma} \left(\ln \frac{b_1}{\langle b \rangle} - \frac{5\sigma^2}{2} \right) \right) \right]; \\ I_{II} &= \frac{\langle b \rangle^{(2n+1)/n}}{2} \exp \left(\frac{(2n+1)(n+1)}{2n^2} \sigma^2 \right) \times \\ &\times \left[\operatorname{erf} \left(\frac{1}{\sqrt{2}\sigma} \left(\ln \frac{b_2}{\langle b \rangle} - \frac{(3n+2)\sigma^2}{2n} \right) \right) - \operatorname{erf} \left(\frac{1}{\sqrt{2}\sigma} \left(\ln \frac{b_1}{\langle b \rangle} - \frac{(3n+2)\sigma^2}{2n} \right) \right) \right]; \\ I_{III} &= \frac{\langle b \rangle^3}{2} \exp(3\sigma^2) \left[1 - \operatorname{erf} \left(\frac{1}{\sqrt{2}\sigma} \left(\ln \frac{b_2}{\langle b \rangle} - \frac{5\sigma^2}{2} \right) \right) \right], \end{aligned} \quad (10)$$

$$\begin{aligned} P_{II} &= \frac{1}{2} \left[\operatorname{erf} \left(\frac{1}{\sqrt{2}\sigma} \left(\ln \frac{b_2}{\langle b \rangle} + \frac{\sigma^2}{2} \right) \right) - \operatorname{erf} \left(\frac{1}{\sqrt{2}\sigma} \left(\ln \frac{b_1}{\langle b \rangle} + \frac{\sigma^2}{2} \right) \right) \right]; \\ P_{III} &= \frac{1}{2} \left[1 - \operatorname{erf} \left(\frac{1}{\sqrt{2}\sigma} \left(\ln \frac{b_2}{\langle b \rangle} + \frac{\sigma^2}{2} \right) \right) \right], \end{aligned} \quad (11)$$

where $\operatorname{erf}(\dots)$ is the error function.

The Eqs. (4-8) of the flow rate are compared with that of a pure power-law fluid (q_{pl}), derived by [25], of parameters m and n i.e. for case 1

$$q_{x,pl} = \frac{n}{2n+1} \left(\frac{p_x}{2^{n+1}m} \right)^{1/n} \langle b \rangle^{(2n+1)/n} \exp \left(\frac{(2n+1)(n+1)\sigma^2}{2n^2} \right), \quad (12)$$

and for case 2

$$q_{y,pl} = \frac{n}{2n+1} \left(\frac{p_y}{2^{n+1}m} \right)^{1/n} \langle b \rangle^{(2n+1)/n} \exp \left(-\frac{(2n+1)(n+1)\sigma^2}{n} \right). \quad (13)$$

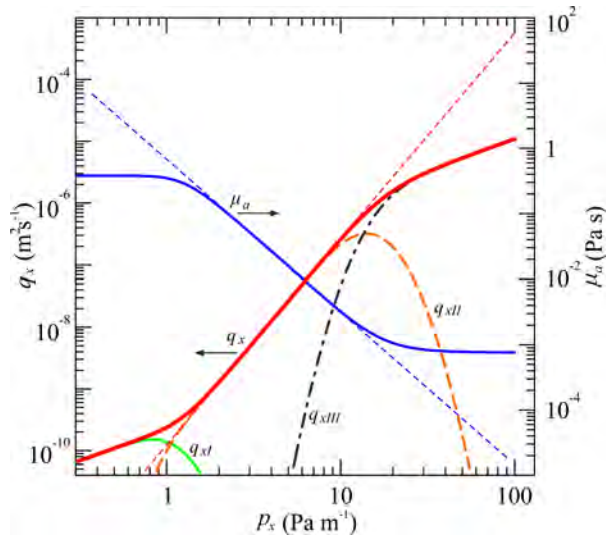


Figure 3: Flowrate and apparent viscosity for case 1 (flow perpendicular to aperture variation) and lognormal aperture distribution. The thick red continuous curve refers to the flowrate (left axis), with the three contributions: the low-shear rate regime q_{xI} (continuous green curve), the mid-shear rate regime q_{xII} (dashed orange curve), the high-shear rate regime q_{xIII} (dash-dot black curve). The blue continuous curve refers to the apparent viscosity (right axis) and the dashed lines refer to the power-law fluid. The parameters are $n = 0.3$, $\sigma = 0.3$, $\langle b \rangle = 0.001$ m, $\mu_0 = 0.5$ Pa s, $\mu_\infty = 0.001$ Pa s, $m = 0.005$ Pa s n .

In Figure 3, flowrate and apparent viscosity versus the pressure gradient are depicted, for lognormal aperture distribution and flow perpendicular to aperture variation (case 1). The contribution of each single flow regime is also represented, in order to quantify their influence on the total flowrate. The presence of three possible flow regime, i.e. (i) low-shear-rate, (II) mid-shear-rate and (III) high-shear-rate allows us to understand why for a certain value of pressure gradient the two models sensibly differ. Clearly, $q_x \rightarrow q_{x,pl}$ for $\mu_0 \rightarrow \infty$ and $\mu_\infty \rightarrow 0$. A similar behavior occurs for different aperture distributions and direction of flowrate (case 2).

The different trends between q_x and $q_{x,pl}$ are showed in Figures 4a - 4f, for lognormal distribution and case 1, with $n = 0.3, 0.5, 0.6$, $\mu_0 = 0.5$ Pas, $\mu_\infty = 0.001$ Pas, and $m = 0.005$ Pas^{*n*}. Figures 4a, 4b, and 4c depict q_x and $q_{x,pl}$ versus p_x for fixed $\sigma = 0.3$; Figures 4d, 4e, 4f do so versus σ for fixed $p_x = 50$ Pa m⁻¹. It is seen that the flowrate for the truncated model is always decidedly smaller than that associated with the pure power-law, except at very low gradient pressure, where the opposite is true. The difference between the two increases as the external pressure gradient and aperture variability become larger or sufficiently small. Increasing the rheological parameter n , the difference between the truncated power law and pure power law model reduces.

In Figure 4a, the truncated power law model, compared with the pure power law model for a fluid with $n = 0.3$, exhibits all flow regimes. Here, it is possible to observe a very small low-shear-rate regime for lower values of pressure gradient, a mid-shear-rate where the two models perfectly match, and a high-shear-rate regime with a lower slope than the pure power law model. Figures 4b and 4c depict the same behavior for different fluids, respectively with $n = 0.5, 0.6$. In these configurations, the low-shear-rate regime is not present, while the high-shear-rate regime is reached for higher values of pressure gradient and the difference between the models is less marked.

Figures 4d, 4e, and 4f show how aperture variability σ influences the flow rate for a given pressure gradient p_x and different fluids. For both models, the flowrate increases with σ , as the parallel arrangement emphasizes the importance of large-aperture channels associated with a larger variability; the truncated model has decidedly smaller flow rates than the pure power-law. The difference between the two models decreases as n increases, until for $n = 0.6$ the difference is very small, and the two models provide identical results in a large range of aperture variability.

Figure 5 shows instead the variation of flowrate with respect to pres-

sure gradient, for case 2 (serial arrangement) and both the truncated and pure power-law models. Figure 5a highlights the behavior of flowrate versus pressure gradient, for $n = 0.3, 0.5, 0.6$, and fixed $\sigma = 0.5$. Here, a monotonic increasing behavior occurs, with a perfect match between truncated and pure power-law model for low values of pressure gradient. For higher values of the gradient, the truncated model presents a lower slope with respect to the pure power law, but this difference is less marked as n increases; in particular, the truncated model assumes almost the same values, irrespective of the type of fluid. For high gradient values, the truncated model has a lower flowrate than the pure power-law, like in case 1. Overall, the difference between the two models strongly depends on the type of fluid, as noted for case 1.

Figure 5b depicts the influence of aperture variability for $\sigma = 0.1$ to 0.5 and fixed $n = 0.3$. For lower values of pressure gradient, the truncated and pure power-law model perfectly match, in particular for small values of aperture variability. For higher values of pressure gradient, the slope for the truncated model is still lower than the pure power-law, as in case 1. For both truncated and pure power-law, the flowrate decreases with increasing aperture variability as the serial arrangement emphasizes the importance of small apertures.

4.2. Gamma distribution

A gamma distribution was adopted by Moreno *et al.* [12] to reproduce the migration of contaminated water in fractured rock in the context of a capillary tube model, and by Tsang *et al.* [13] for one-dimensional channels. Its probability distribution function is given by

$$f(b) = \frac{1}{\Gamma(d)} \frac{b^{d-1}}{b_g^d} \exp\left(-\frac{b}{b_g}\right), \quad (14)$$

with the two parameters b_g (geometric mean) and d . For larger values of d , the gamma distribution tends to the normal one. The arithmetic mean and the variance of b are given by $\langle b \rangle = b_g d$; $\sigma_b^2 = b_g^2 d = \langle b \rangle^2 / d$. Utilizing Eqs. (4)-(5) with Equation(6) gives for the factors P_{II} , P_{III} and I_j ($j = I, II, III$)

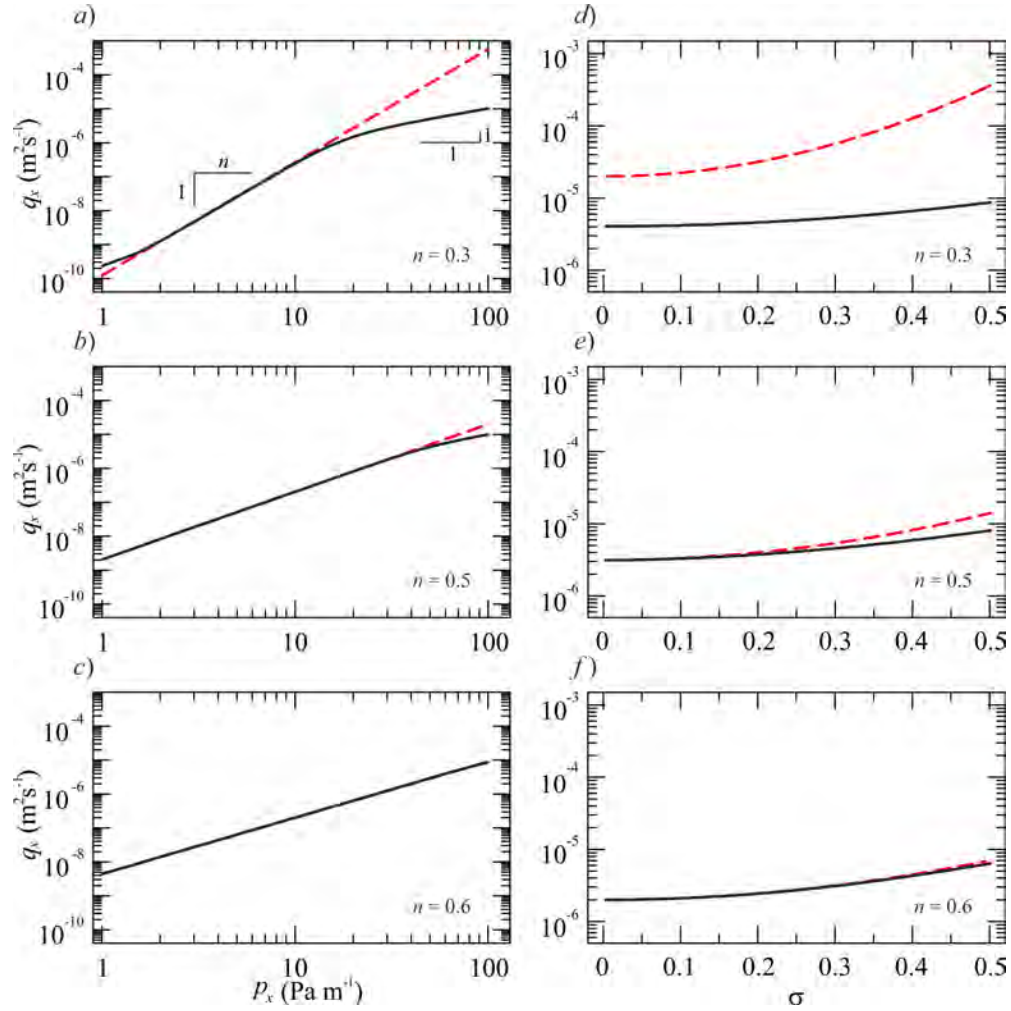


Figure 4: Flowrate for case 1 (flow perpendicular to aperture variation) and lognormal aperture distribution. *a-b-c*) Flowrate vs pressure gradient for $n = 0.3, 0.5, 0.6$, $\sigma = 0.3$; *d-e-f*) flowrate vs σ for $n = 0.3, 0.5, 0.6$, $p_x = 50 \text{ Pa m}^{-1}$. The other parameters are $\langle b \rangle = 0.001 \text{ m}$, $\mu_0 = 0.5 \text{ Pa s}$, $\mu_\infty = 0.001 \text{ Pa s}$, $m = 0.005 \text{ Pa s}^n$. The dashed lines refer to the power-law relationships, the continuous lines refer to the truncated power-law relationship.

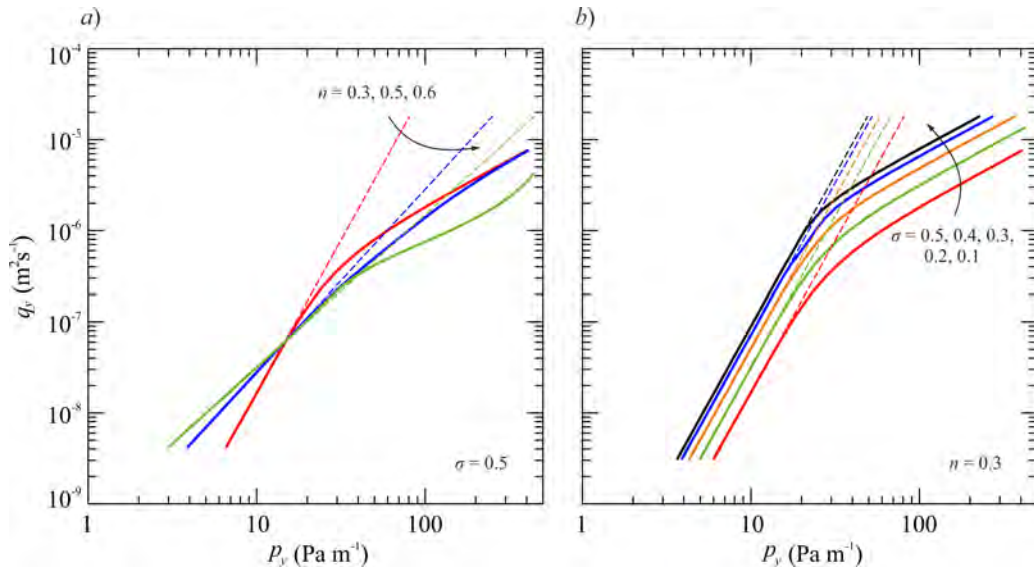


Figure 5: Flowrate for case 2 (flow parallel to aperture variation), lognormal distribution. *a*) Flowrate vs pressure gradient for $n = 0.3, 0.5, 0.6$, $\sigma = 0.5$; *b*) flowrate vs pressure gradient for $\sigma = 0.1(0.1)0.5$, $n = 0.3$. The other parameters are $\langle b \rangle = 0.001$ m, $\mu_0 = 0.5$ Pas, $\mu_\infty = 0.001$ Pas, $m = 0.005$ Pas n . The dashed lines refer to the power-law relationships, the continuous lines refer to the truncated power-law relationship.

the following expressions:

$$\begin{aligned}
 I_I &= \frac{\langle b \rangle^3}{\Gamma(d)d^3} \gamma\left(d+3, \frac{db_1}{\langle b \rangle}\right); \\
 I_{II} &= \frac{\langle b \rangle^{(2n+1)/n}}{\Gamma(d)d^{(2n+1)/n}} \left[\Gamma\left(d + \frac{2n+1}{n}, \frac{db_1}{\langle b \rangle}\right) - \Gamma\left(d + \frac{2n+1}{n}, \frac{db_2}{\langle b \rangle}\right) \right]; \\
 I_{III} &= \frac{\langle b \rangle^3}{\Gamma(d)d^3} \Gamma\left(d+3, \frac{db_2}{\langle b \rangle}\right),
 \end{aligned} \tag{15}$$

$$\begin{aligned}
 P_{II} &= \frac{1}{\Gamma(d)} \left[\Gamma\left(d, \frac{db_1}{\langle b \rangle}\right) - \Gamma\left(d, \frac{db_2}{\langle b \rangle}\right) \right]; \\
 P_{III} &= \frac{1}{\Gamma(d)} \Gamma\left(d, \frac{db_2}{\langle b \rangle}\right),
 \end{aligned} \tag{16}$$

where $\Gamma(z) = \int_0^\infty e^{-t} t^{z-1} dt$ is the gamma function, $\gamma(\alpha, x) = \int_0^x e^{-t} t^{\alpha-1} dt = \Gamma(\alpha) - \Gamma(\alpha, x)$ the lower incomplete gamma function, and $\Gamma(\alpha, x) = \int_x^\infty e^{-t} t^{\alpha-1} dt$ the upper incomplete gamma function. The expression of the flowrate given by Equation (4) with Eqs. (12) and (13) is compared with that of a pure power-law (q_{pl}) fluid of parameters m and n [25], i.e. for case 1:

$$q_{x,pl} = \frac{n}{2n+1} \left(\frac{p_x}{2^{n+1}m} \right)^{1/n} \left(\frac{\langle b \rangle}{d} \right)^{(2n+1)/n} \frac{\Gamma\left(d + \frac{2n+1}{n}\right)}{\Gamma(d)}, \tag{17}$$

while for case 2

$$q_{y,pl} = \frac{n}{2n+1} \left(\frac{p_y}{2^{n+1}m} \right)^{1/n} \left(\frac{\langle b \rangle}{d} \right)^{(2n+1)/n} \left[\frac{\Gamma(d)}{\Gamma(d-2n-1)} \right]^{1/n}. \tag{18}$$

The latter expression is valid only for $d > 2n + 1$. Figures 6 and 7 depict the comparison between the truncated and pure power-law models, drawn for both lognormal and gamma distributions, for case 1 and case 2, respectively. Here, the two distributions are characterized by the same first two moments. In particular, the parameter d of the gamma distribution is derived by the variance of $\ln b$, σ , previously converted in σ_b , i.e. [13]

$$\sigma_b^2 = \langle b \rangle^2 [\exp(\ln 10 \sigma)^2 - 1]. \tag{19}$$

The two distributions differ only by the third and fourth moment. For $\sigma = 0.1$, the skewness is 0.47 for gamma distribution and 0.30 for lognormal, while

kurtosis is 3.32 for gamma and 3.16 for lognormal distribution; for $\sigma = 0.2$, the skewness is 0.97 for gamma distribution and 0.61 for lognormal, while kurtosis is 4.42 for gamma and 3.68 for lognormal distribution.

Figure 6, drawn for the parallel arrangement, shows that the models with the two different distributions and with TPL have a similar trend. The slope of the $q_x - p_x$ relationship for the truncated model for both distributions is lower compared with the pure power-law, for high and low values of pressure gradient. The lognormal distribution consistently shows a lower flowrate than the gamma distribution for the same pressure gradient and aperture variability, due to the differences in the distribution shape; the difference in flowrate between distributions increases with increasing aperture variability.

Figure 7, drawn for the serial arrangement, shows that for the same values of pressure gradient, the pure power law model for lognormal distribution has a higher flowrate than the gamma distribution, both for $\sigma = 0.1$ and $\sigma = 0.2$. For intermediate pressure gradient, all distributions show a good agreement of the flowrate for the truncated power law and for the pure power law model. Again, the differences between the power law and the truncated power law models become evident whenever the flowrate is in the regime controlled by the high and the low shear rate plateaus.

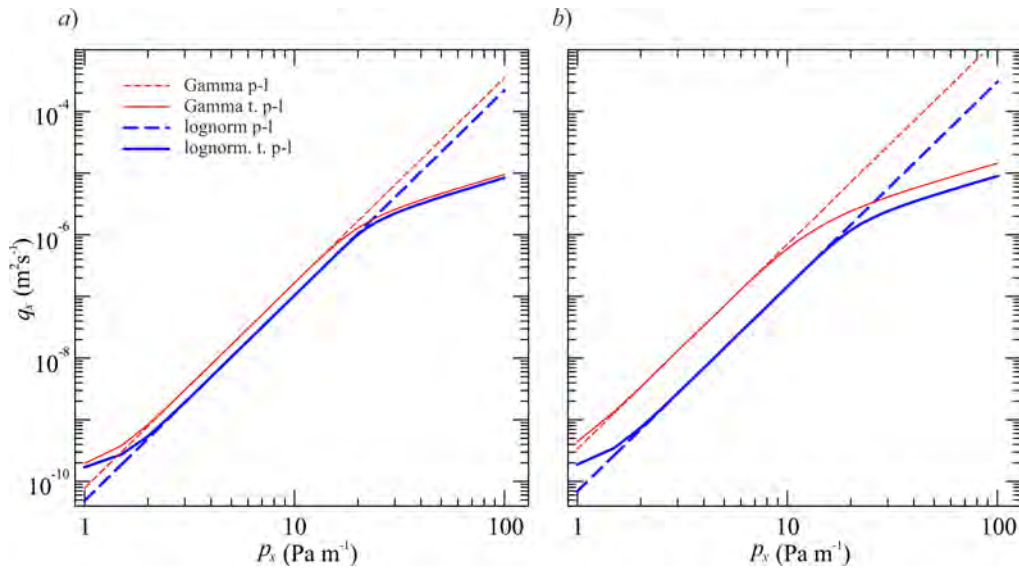


Figure 6: Flowrate for case 1 (flow perpendicular to aperture variation), comparison between lognormal and gamma distributions. *a*) Flowrate vs pressure gradient for $\sigma = 0.1$ (lognormal) and $d = 18.37$ (gamma); *b*) flowrate vs pressure gradient for $\sigma = 0.2$ and $d = 4.23$. The other parameters are $n = 0.3$, $\langle b \rangle = 0.001$ m, $\mu_0 = 0.5$ Pas, $\mu_\infty = 0.001$ Pas, $m = 0.005$ Pas n . The dashed lines refer to the power-law relationships, the continuous lines refer to the truncated power-law relationship.

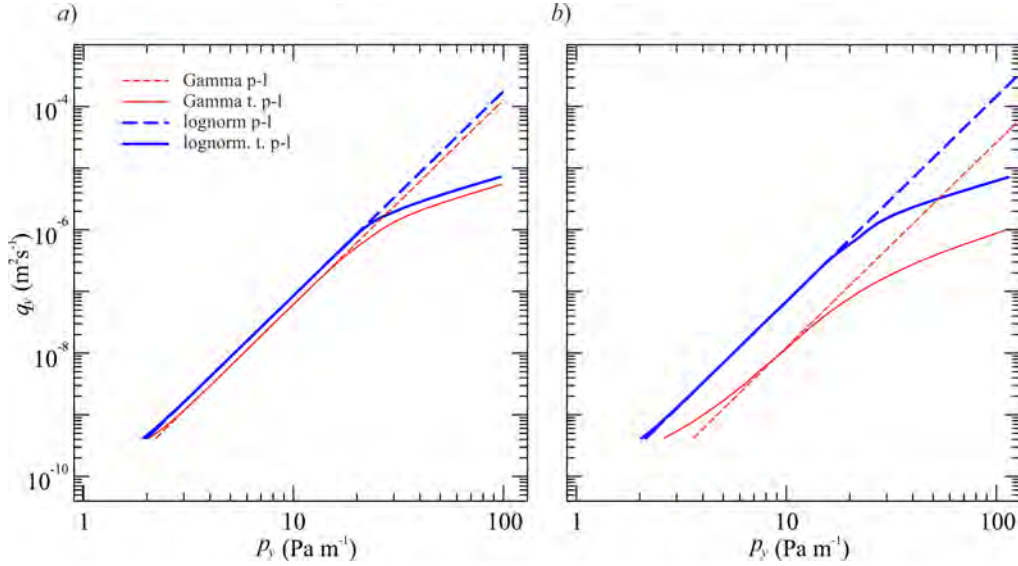


Figure 7: Flowrate for case 2 (flow parallel to aperture variation), comparison between lognormal and gamma distributions. For caption see Figure 6.

5. Deterministic aperture variation

We consider a constant aperture with a sinusoidal perturbation as “rough-walled” fracture [37, 26], as depicted in Figure 8:

$$b(y) = \langle b \rangle [1 + \delta \sin(2\pi y/\lambda)] \quad (20)$$

where $\langle b \rangle$ is the mean aperture, δ is the magnitude of the “roughness”, and λ is the wavelength of the aperture oscillations. Upon comparing the limiting aperture values b_1 , b_2 for a given pressure gradient separating the different flow regimes for the truncated power-law model, and the minimum, mean and maximum aperture values $b_{min} = \langle b \rangle(1 - \delta)$, $\langle b \rangle$, and $b_{max} = \langle b \rangle(1 + \delta)$, it is seen that ten possible combinations arise, as reported in Table 1. The standard deviation of the aperture distribution σ_b is related to the parameter δ by

$$\sigma_b = \frac{\delta \langle b \rangle}{\sqrt{2}}. \quad (21)$$

In the following we compare the behavior, in terms of flowrate for a given value of the pressure gradient, of a deterministic and stochastic aperture variation, both for flow parallel to constant aperture channels (case 1), and

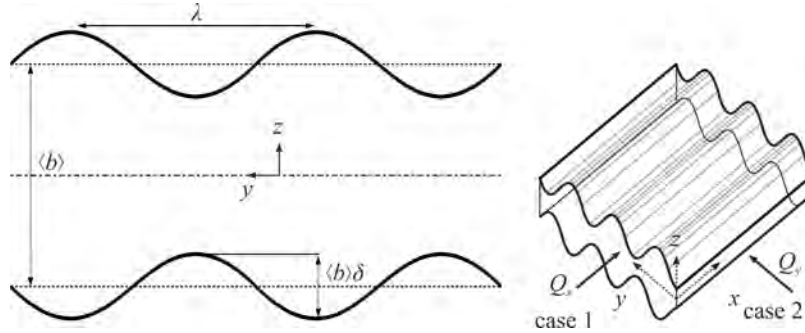


Figure 8: Rough-walled fracture profile adopted for the deterministic formulation.

flow perpendicular to constant aperture channels (case 2). The lognormal distribution is adopted for the stochastic variation, hence the quantities I_I , I_{II} , and I_{III} and P_{II} , and P_{III} are those reported in Eqs. (10) and (11). The same quantities, evaluated for the deterministic variation, are listed in Tables 2 and 3 of Appendix B for all the possible combinations presented in Table 1. In Figure 9a for case 1, a fluid with rheology index $n = 0.5$ is considered, the roughness is taken to be $\delta = 0.2$, and the same variance is considered for both types of variation. The flowrate increases with the pressure gradient, and the agreement between deterministic and stochastic model is good. The comparison between the two models, for case 1, is also shown as a function of σ in Figure 9b, for $n = 0.5$, and $p_x = 30 \text{ Pa m}^{-1}$. Here, the deterministic model tends to predict higher values of the flowrate q_x than the stochastic approach for increasing values of log aperture standard deviation. Figure 10a depicts the comparison between deterministic and stochastic aperture variation for case 2, with $n = 0.3$, and $\delta = 0.2$. It is seen that the stochastic variation tends to overestimate the flowrate for increasing pressure gradient, while for lower values of p_x , the agreement between the two models is quite good. This trend is confirmed by Figure 10b, drawn for $p_x = 0.5 \text{ Pa m}^{-1}$, where the deterministic model returns flowrates increasingly lower than the stochastic as σ increases.

6. Discussion and conclusions

We derived analytical models for flow of non-Newtonian fluids in uneven channels simulating natural or artificial rock fractures. Our approach couples

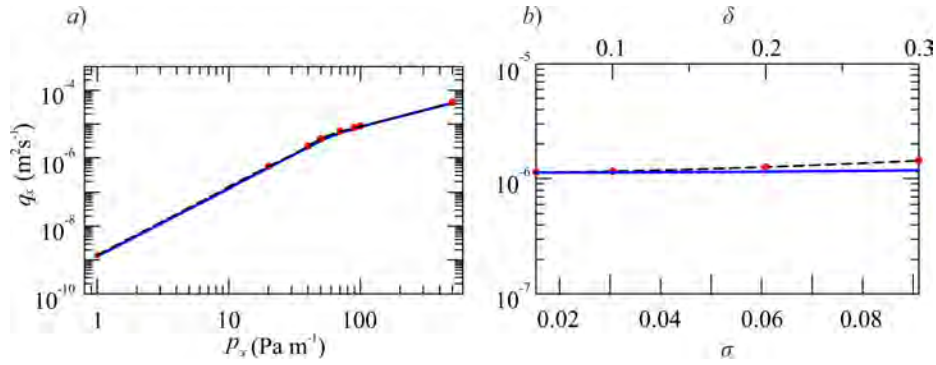


Figure 9: Comparison of deterministic (red dots) and stochastic approach (blue line), for case 1 (flow perpendicular to aperture variation). *a*) Flowrate versus pressure gradient, for $\delta = 0.2$, and $n = 0.5$; *b*) flowrate versus standard deviation for $p_x = 30 \text{ Pa m}^{-1}$, and $n = 0.5$. The other parameters are $\langle b \rangle = 0.001 \text{ m}$, $\mu_0 = 0.5 \text{ Pa s}$, $\mu_\infty = 0.001 \text{ Pa s}$, $m = 0.005 \text{ Pa s}^n$.

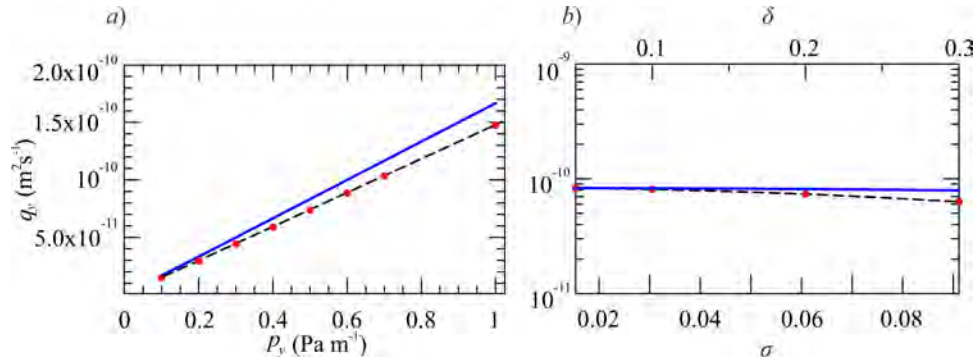


Figure 10: Comparison of deterministic (red dots) and stochastic approach (blue line), for case 2 (flow parallel to aperture variation). *a*) Flowrate versus pressure gradient, for $\delta = 0.2$ and $n = 0.3$; *b*) flowrate versus standard deviation for $p_x = 0.5 \text{ Pa m}^{-1}$, and $n = 0.3$. The other parameters are $\langle b \rangle = 0.001 \text{ m}$, $\mu_0 = 0.5 \text{ Pa s}$, $\mu_\infty = 0.001 \text{ Pa s}$, $m = 0.005 \text{ Pa s}^n$.

Combinations

1	$b_1 < b_2 < b_{min} < b_{max}$	
2	$b_1 < b_{min} < b_2 < b_{max},$	$\langle b \rangle > b_2$
3	$b_1 < b_{min} < b_2 < b_{max},$	$\langle b \rangle < b_2$
4	$b_1 < b_{min} < b_{max} < b_2$	
5	$b_{min} < b_1 < b_{max} < b_2,$	$\langle b \rangle < b_1$
6	$b_{min} < b_1 < b_{max} < b_2,$	$\langle b \rangle > b_1$
7	$b_{min} < b_{max} < b_1 < b_2$	
8	$b_{min} < b_1 < b_2 < b_{max},$	$\langle b \rangle < b_1 < b_2$
9	$b_{min} < b_1 < b_2 < b_{max},$	$b_1 < \langle b \rangle < b_2$
10	$b_{min} < b_1 < b_2 < b_{max},$	$b_1 < b_2 < \langle b \rangle$

Table 1: Combinations of deterministic aperture variations.

a four-parameter rheological model, the truncated power-law (TPL), with a stochastic variation of the aperture field along a 1-D channel according to a generic probability distribution function (pdf); three different cases are considered including a deterministic variation of sinusoidal shape.

Starting from the solution valid for TPL parallel plate flow, which incorporates three possible flow regimes, the conductance of the channel is determined as a function of rheological fluid parameters, geometry, and the pdf of the aperture distribution. Two limit cases providing an upper and lower bound to the flowrate under an assigned pressure gradient are considered, the parallel (PA) and serial (SA) arrangements, corresponding respectively to an external pressure gradient perpendicular or parallel to aperture variation.

Results for the simpler, two-parameter power-law (PL) rheological model provide the benchmark to discern the impact of the adoption of a more realistic rheological model on the conductance. On one hand, the parallel arrangement emphasizes the importance of large-aperture channels; here the TPL has a smaller conductance than the PL, the difference increasing with aperture variability and pressure gradient and decreasing with flow behavior index. On the other hand, small apertures along the channels play a crucial role in the serial arrangement; here results for the TPL and PL agree for intermediate gradients and differ for larger/smaller ones, when the conductance of the TPL is lower/higher than the PL. The differences between TPL and PL again increase with aperture variability and decrease with flow behavior index.

The impact of the specific pdf adopted for the aperture variation is moderate, with the first two moments being equal. The difference in conductance is an increasing function of aperture variability and depends on the third and fourth moment of the distribution. Specifically, higher values of skewness and kurtosis imply a smaller conductance for the parallel and a larger conductance for the serial arrangement. When a deterministic sinusoidal aperture variation is considered, all trends valid for stochastic variations are confirmed. Differences in conductance with stochastic aperture variation increase with pressure gradient and aperture variability, and are of opposite sign depending on the aperture arrangement.

Our model reveals the coupled effect of aperture heterogeneity and a realistic rheological equation for non-Newtonian fluid flow in rock fractures, a topic of interest in hydraulic fracturing, drilling, EOR, and environmental modelling and remediation. The relevance of rheological properties of real fluids and of the stochastic nature of the fractures suggest a more in

depth analysis of the coupling effects. Polymer flooding is often used for EOR since the addition of polymers to the injected brine favors an improved sweep, a reduction of fingering with a more stable displacement. Whilst EOR polymers in a rheometer display Newtonian and shear thinning behaviour, approximated by a TPL relationship, in the field polymers show a quite complex behavior partially captured in the present model, dictated by the flow geometry driven by fractures networks. Recovery mechanism in fractured reservoirs (carbonate reservoirs usually are extensively fractured but show a low porosity) is strongly influenced by the fractures, which show a well different transmissivity than the matrix and carry most of the flow limiting a large differential pressure and the efficiency of recovery. The nature of the fluid and the characteristics of the fractures counteract this negative aspect. As a matter of evidence, the TPL fluids show a reduction (increment) of flowrate at high (low) shear rates for a given pressure gradient with respect to the PL fluids. The relevance of this reduction/increment and its onset are controlled by the Newtonian plateaus and by the fractures parameters, mainly the average and the variance of the aperture of the fractures.

Results suggest to investigate further this coupling expanding the investigation to two-dimensional modeling of the aperture variation, inclusion of local pressure losses, and adoption of yield-stress rheological models or more complex models. A further element adding complexity to the model is shear-thickening behaviour due to elongation of the polymer molecules, typical of flow in capillary tubes with a sharp contraction [38]. At large flowrates, depending on the fractures characteristics, an elongational contribution adds up to the total pressure drop, showing a shear-thickening effect which can be included in the present model.

7. Appendix A - Alternative formulation for serial configuration

The pressure gradient can be estimated as the inverse of Eqs.(2-2c). We notice that while for a given pressure gradient the condition $b < b_1$ (and $b_1 < b < b_2$, $b > b_2$) must be satisfied in order to guarantee a low-shear, $\dot{\gamma} \leq \dot{\gamma}_1$ (intermediate $-\dot{\gamma}_1 \leq \dot{\gamma} \leq \dot{\gamma}_2$ and high-shear - $\dot{\gamma} \geq \dot{\gamma}_2$) regime, for a given inflow rate q_y the new conditions are

$$p_{yI}(b) = q_{yI}^{-1} \equiv \frac{12\mu_0 q_y}{b^3} \quad \text{for } b > b'_1 \equiv \sqrt{\frac{6q_y}{\dot{\gamma}_1}}; \quad (22a)$$

$$p_{yII}(b) = q_{yII}^{-1} \quad \text{for } b'_2 < b < b'_1; \quad (22b)$$

$$p_{yIII}(b) = q_{yIII}^{-1} \quad \text{for } b < b'_2 \equiv \sqrt{\frac{q_y}{\frac{m\dot{\gamma}_2^n}{6\mu_\infty} - \frac{a}{4m^2\dot{\gamma}_2^{2n}}}}, \quad (22c)$$

$$a = \frac{2(1-n)m^{3/(1-n)}}{3(2n+1)} \left(\frac{1}{\mu_\infty^{(2n+1)/(1-n)}} - \frac{1}{\mu_0^{(2n+1)/(1-n)}} \right),$$

with $b'_2 < b'_1$. The inverse functions for the low-shear regime, $p_{yI} = q_{yI}^{-1}$, and the high-shear regime, $p_{yIII} = q_{yIII}^{-1}$, can be found analytically. At intermediate regime the inverse function $p_{yII} = q_{yII}^{-1}$ can be found analytically only for $n = 1/2, 1/4, 1/6$, while in general a numerical inversion is requested. We notice that for $n = 1/2$ the inverse function has two real-valued positive branches. This mathematical aspect could bring to hysteretic behaviour of the flow in the fracture, with different paths in the space $p_y - q_y$ according to the initial state: (i) a low pressure gradient regime and (ii) a high pressure gradient regime for the same flow rate. However, upon introduction of further dissipative effects, mainly due to expansion of the troughs, the hysteresis should be mitigated and eventually cancelled. We will not pursue this aspect, which requires an experimental validation, and we choose the branch of the inverse function corresponding to the high pressure gradient regime. Taking the limit as $N_j \rightarrow \infty$, the length of each cell tends to zero and the discrete aperture variation to a continuous one; then under ergodicity, and exploiting the previous relationships, Equation (7) gives for the mean pressure gradient in the y direction the expression

$$p_y = \int_{b'_1}^{\infty} p_{yI} f(b) db + \int_{b'_2}^{b'_1} p_{yII} f(b) db + \int_0^{b'_2} p_{yIII} f(b) db. \quad (23)$$

8. Appendix B - Quantities of interest for deterministic aperture variation

For the deterministic, sinusoidal aperture variation of Section 5, Table 2 reports the integrals I_I, I_{II}, I_{III} , while Table 3 shows P_{II}, P_{III} for the different combinations reported in Table 1. In both tables, consider $\theta_i = \arcsin \left[\frac{1}{\delta} \left(\frac{b_i}{\langle b \rangle} - 1 \right) \right]$.

Combinations	I_I	I_{II}	I_{III}
1	0	0	$\frac{\delta_1^3}{2\pi} (1 + \frac{3\delta^2}{2})$
2	0	$\frac{\delta_1^{2n+1}}{3\pi-2\delta_1} \int_{\theta_2}^{\theta_1} \frac{r^{3n-\theta_1}}{r-\theta_2} (1 + \delta \sin \theta)^{\frac{2n+1}{\pi}} d\theta$	$(\theta)^3 \left[\frac{1}{\theta_2} \int_{\theta_2}^{\theta_1} r^{\theta_2} (1 + \delta \sin \theta)^3 d\theta + \frac{1}{\theta_1-\theta_2} \int_{\theta_1-\theta_2}^{2\pi} r^{2\pi} (1 + \delta \sin \theta)^3 d\theta \right]$
3	0	$(\theta)^{\frac{2n+1}{\pi}} \left[\frac{1}{\theta_2} \int_{\theta_2}^{\theta_1} r^{\theta_2} (1 + \delta \sin \theta)^{\frac{2n+1}{\pi}} d\theta + \frac{1}{\pi-\theta_2} \int_{\pi-\theta_2}^{2\pi} r^{2\pi} (1 + \delta \sin \theta)^{\frac{2n+1}{\pi}} d\theta \right]$	$\frac{\delta_1^{2n+1}}{\pi-2\theta_2} \int_{\theta_2}^{\theta_1} r^{3n-\theta_1} (1 + \delta \sin \theta)^{\frac{2n+1}{\pi}} d\theta$
4	0	$(\theta)^{\frac{2n+1}{\pi}} \int_{\theta_2}^{\theta_1} r^{2\pi} (1 + \delta \sin \theta)^{\frac{2n+1}{\pi}} d\theta$	0
5	$(\theta)^3 \left[\frac{1}{\theta_2} \int_{\theta_2}^{\theta_1} r^{\theta_2} (1 + \delta \sin \theta)^3 d\theta + \frac{1}{\pi-2\theta_1} \int_{\pi-2\theta_1}^{2\pi} r^{2\pi} (1 + \delta \sin \theta)^3 d\theta \right]$	$\frac{\delta_1^{2n+1}}{\pi-2\theta_1} \int_{\theta_2}^{\theta_1} r^{3n-\theta_1} (1 + \delta \sin \theta)^{\frac{2n+1}{\pi}} d\theta$	0
6	$\frac{\delta_1^{3n-\theta_1}}{3\pi-2\theta_1} \int_{\theta_2}^{\theta_1} r^{3n-\theta_1} (1 + \delta \sin \theta)^3 d\theta$	$(\theta)^{\frac{2n+1}{\pi}} \left[\frac{1}{\theta_2} \int_{\theta_2}^{\theta_1} r^{\theta_2} (1 + \delta \sin \theta)^{\frac{2n+1}{\pi}} d\theta + \frac{1}{\theta_1-\theta_2} \int_{\theta_1-\theta_2}^{2\pi} r^{2\pi} (1 + \delta \sin \theta)^{\frac{2n+1}{\pi}} d\theta \right]$	0
7	$\frac{\delta_1^3}{2\pi} (1 + \frac{3\delta^2}{2})$	0	0
8	$(\theta)^3 \left[\frac{1}{\theta_2} \int_{\theta_2}^{\theta_1} r^{\theta_2} (1 + \delta \sin \theta)^3 d\theta + \frac{1}{\pi-2\theta_1} \int_{\pi-2\theta_1}^{2\pi} r^{2\pi} (1 + \delta \sin \theta)^3 d\theta \right]$	$\frac{\delta_1^{2n+1}}{\theta_2-\theta_1} \left[\int_{\theta_2}^{\theta_1} r^{\theta_2} (1 + \delta \sin \theta)^{\frac{2n+1}{\pi}} d\theta + \int_{\pi-2\theta_1}^{\pi-\theta_2} r^{2\pi} (1 + \delta \sin \theta)^{\frac{2n+1}{\pi}} d\theta \right]$	$\frac{\delta_1^{3n-\theta_1}}{\pi-2\theta_2} \int_{\theta_2}^{\theta_1} r^{3n-\theta_1} (1 + \delta \sin \theta)^3 d\theta$
9	$\frac{\delta_1^{3n-\theta_1}}{3\pi-2\theta_1} \int_{\theta_2}^{\theta_1} r^{3n-\theta_1} (1 + \delta \sin \theta)^3 d\theta$	$(\theta)^{\frac{2n+1}{\pi}} \left[\frac{1}{\theta_2} \int_{\theta_2}^{\theta_1} r^{\theta_2} (1 + \delta \sin \theta)^{\frac{2n+1}{\pi}} d\theta + \frac{1}{\theta_1-\theta_2} \int_{\theta_1-\theta_2}^{2\pi} r^{2\pi} (1 + \delta \sin \theta)^{\frac{2n+1}{\pi}} d\theta + \frac{1}{\theta_1-\theta_2} \int_{\theta_1-\theta_2}^{2\pi} r^{2\pi} (1 + \delta \sin \theta)^{\frac{2n+1}{\pi}} d\theta \right]$	$\frac{\delta_1^{3n-\theta_1}}{\pi-2\theta_2} \int_{\theta_2}^{\theta_1} r^{3n-\theta_1} (1 + \delta \sin \theta)^3 d\theta$
10	$\frac{\delta_1^{3n-\theta_1}}{3\pi-2\theta_1} \int_{\theta_2}^{\theta_1} r^{3n-\theta_1} (1 + \delta \sin \theta)^3 d\theta$	$\frac{\delta_1^{2n+1}}{\theta_1-\theta_2} \left[\int_{\theta_2}^{\theta_1} r^{\theta_2} (1 + \delta \sin \theta)^{\frac{2n+1}{\pi}} d\theta + \int_{\theta_1-\theta_2}^{\pi-\theta_2} r^{2\pi} (1 + \delta \sin \theta)^{\frac{2n+1}{\pi}} d\theta \right]$	$(\theta)^3 \left[\frac{1}{\theta_2} \int_{\theta_2}^{\theta_1} r^{\theta_2} (1 + \delta \sin \theta)^3 d\theta + \frac{1}{\theta_1-\theta_2} \int_{\theta_1-\theta_2}^{2\pi} r^{2\pi} (1 + \delta \sin \theta)^3 d\theta \right]$

 Table 2: Integrals I_I , I_{II} , and I_{III} for the deterministic case.

<i>Combinations</i>	P_{II}	P_{III}
1	0	1
2	$\left \frac{\pi - 2\theta_2}{2\pi} \right $	$1 - \left \frac{\pi - 2\theta_2}{2\pi} \right $
3	$\left \frac{\pi - 2\theta_2}{2\pi} \right $	$1 - \left \frac{\pi - 2\theta_2}{2\pi} \right $
4	1	0
5	$\left \frac{\pi - 2\theta_1}{2\pi} \right $	0
6	$\left \frac{\pi - 2\theta_1}{2\pi} \right $	0
7	0	0
8	$\left \frac{\pi - 2\theta_2}{2\pi} \right $	$1 - \sum_{k=1}^2 \left \frac{\pi - 2\theta_k}{2\pi} \right $
9	$\left \frac{\pi - 2\theta_2}{2\pi} \right $	$1 - \sum_{k=1}^2 \left \frac{\pi - 2\theta_k}{2\pi} \right $
10	$\left \frac{\pi - 2\theta_2}{2\pi} \right $	$1 - \sum_{k=1}^2 \left \frac{\pi - 2\theta_k}{2\pi} \right $

Table 3: P_{II} , and P_{III} for the deterministic case.

References

- [1] A. M. Linkov, On comparison of thinning fluids used for hydraulic fracturing, *International Journal of Engineering Science* 10 (2014) 14–23. doi:10.1016/j.ijengsci.2013.12.005.
- [2] S. A. Boronin, A. A. Osiptsov, J. Descroches, Displacement of yield-stress fluids in a fracture, *International Journal of Multiphase Flow* 76 (2015) 47–63. doi:10.1016/j.ijmultiphaseflow.2015.07.001.
- [3] J. P. Morris, G. G. Chochua, A. V. Bogdan, An efficient non-Newtonian fluid-flow simulator for variable aperture fractures, *The Canadian Journal of Chemical Engineering* 93 (2015) 1902–1915. doi:10.1002/cjce.22314.
- [4] M. Ozdemirtas, E. Kuru, T. Babadagli, Experimental investigation of borehole ballooning due to flow of non-Newtonian fluids into fractured rock, *International Journal of Rock Mechanics and Mining Sciences* 47 (2010) 1200–1206. doi:10.1016/j.ijrmms.2010.07.002.
- [5] J. Huang, D. V. Griffiths, S. W. Wong, Characterizing natural-fracture permeability from mud-loss data, *SPE Journal* 16 (2011) 111–114. doi:10.2118/139592-PA.
- [6] H. Auradou, A. Boschan, R. Chertcoff, S. Gabbanelli, J. P. Hulin, I. Ippolito, Enhancement of velocity contrasts by shear-thinning solutions flowing in a rough fracture, *Journal of Non-Newtonian Fluid Mechanics* 153 (2008) 53–61. doi:10.1016/j.jnnfm.2007.11.008.
- [7] R. Medina, J. E. Elkhoury, J. P. Morris, R. Prioul, J. Desroches, R. L. Detwiler, Flow of concentrated suspensions through fractures: small variations in solid concentration cause significant in-plane velocity variations, *Geofluids* 15 (2015) 24–36. doi:10.1111/gfl.12109.
- [8] P. M. Adler, J. F. Thovert, V. M. Mourzenko, *Fractured Porous Media*, Oxford University Press, 2002.
- [9] C. Neuzil, J. Tracy, Flow through fracture, *Water Resources Research* 17(1) (1981) 191–199. doi:10.1029/WR017i001p00191.

- [10] Y. Tsang, C. Tsang, Channel model of flow through fractured media, *Water Resources Research* 23 (3) (1987) 467–479. doi:10.1029/WR023i003p00467.
- [11] Y. W. Tsang, The effect of tortuosity on fluid flow through a single fracture, *Water Resources Research* 20(9) (1984) 1209–1215. doi:10.1029/WR020i009p01209.
- [12] L. Moreno, Y. W. Tsang, C. F. Tsang, F. V. Hale, I. Neretnieks, Flow and tracer transport in a single fracture: a stochastic model and its relation to some field observations, *Water Resources Research* 24(12) (1988) 2033–2048. doi:10.1029/WR024i012p02033.
- [13] Y. W. Tsang, C. F. Tsang, I. Neretnieks, L. Moreno, Flow and tracer transport in fractured media: a variable aperture channel model and its properties, *Water Resources Research* 24(12) (1988) 2049–2060. doi:10.1029/WR024i012p02049.
- [14] Y. W. Tsang, C. F. Tsang, Flow channeling in a single fracture as a two-dimensional strongly heterogeneous permeable medium, *Water Resources Research* 25(9) (1989) 2076–2080. doi:10.1029/WR025i009p02076.
- [15] S. R. Brown, Fluid flow through rock joints: the effect of surface roughness, *Journal of Geophysical Research: Solid Earth* 92(B2) (1987) 1337–1347. doi:10.1029/JB092iB02p01337.
- [16] V. V. Mourzenko, J. F. Thovert, P. Adler, Permeability of self-affine fractures, *Transport in Porous Media* 45(1) (2001) 89–103. doi:10.1023/A:1011859722257.
- [17] Y. Yan, J. Koplik, Flow of power-law fluids in self-affine fracture channels, *Physical Review E* 77 (2008) 036315. doi:10.1103/PhysRevE.77.036315.
- [18] L. Talon, H. Auradou, A. Hansen, Permeability of self-affine aperture fields, *Physical Review E* 82 (2010) 046108. doi:10.1103/PhysRevE.82.046108.

- [19] R. W. Zimmerman, G. S. Bodvarsson, Hydraulic conductivity of rock fractures, *Transport in Porous Media* 23 (1996) 1–30. doi:10.1007/BF00145263.
- [20] P. M. Adler, J. F. Thovert, *Fractures and fracture networks*, Kluwer, 1999.
- [21] B. Berkowitz, Characterizing flow and transport in fractured geological media: A review, *Advances in Water Resources* 25 (2002) 861–884. doi:10.1016/S0309-1708(02)00042-8.
- [22] M. Sahimi, *Flow and transport in porous media and fractured rock: from classical methods to modern approaches*, 2nd Edition, Wiley, 2011.
- [23] S. E. Silliman, An interpretation of the difference between aperture estimates derived from hydraulic and tracer tests in a single fracture, *Water Resources Research* 25 (1989) 2275–2283. doi:10.1029/WR025i010p02275.
- [24] Y. W. Tsang, Usage of "Equivalent Apertures" for rock fractures as derived from hydraulic and tracer tests, *Water Resources Research* 28 (1992) 1451–1455. doi:10.1029/92WR00361.
- [25] V. Di Federico, Non-Newtonian flow in a variable aperture fracture, *Transport in Porous Media* 30 (1998) 75–86. doi:10.1023/A:1006512822518.
- [26] V. Di Federico, Estimates of equivalent aperture for non-Newtonian flow in a rough-walled fracture, *International Journal of Rock Mechanics and Mining Sciences and Geomechanics Abstracts* 34 (1997) 1133–1137. doi:10.1016/S1365-1609(97)90205-7.
- [27] V. Di Federico, On non-Newtonian fluid flow in rough fractures, *Water Resources Research* 37 (2001) 2425–2430. doi:10.1029/2001WR000359.
- [28] A. Lavrov, Redirection and channelization of power-law fluid flow in a rough walled fracture, *Chemical Engineering Science* 99 (2013b) 81–88. doi:10.1016/j.ces.2013.05.045.
- [29] A. Lavrov, Radial flow of non-Newtonian power-law fluid in a rough-walled fracture: Effect of fluid rheology, *Transport in Porous Media* 105 (2014) 559–570. doi:10.1007/s11242-014-0384-6.

- [30] A. Lavrov, Numerical modeling of steady-state flow of a non-Newtonian power-law fluid in a rough-walled fracture, *Computers and Geotechnics* 50 (2013a) 101–109. doi:10.1016/j.compgeo.2013.01.004.
- [31] S. P. Neuman, Trends, prospects and challenges in quantifying flow and transport through fractured rocks, *Hydrogeology Journal* 13 (2005) 124–147. doi:10.1007/s10040-004-0397-2.
- [32] A. Roustaei, T. Chevalier, L. Talon, I. Frigaard, Non-Darcy effects in fracture flows of a yield stress fluid, *Journal of Fluid Mechanics* 805 (2016) 222–261. doi:10.1017/jfm.2016.491.
- [33] M. Perkowska, M. Wrobel, G. Mishuris, Universal hydrofracturing algorithm for shear-thinning fluids: Particle velocity based simulation, *Computers and Geotechnics* 71 (2016) 310–337. doi:10.1016/j.compgeo.2015.10.005.
- [34] A. Lavrov, Flow of truncated power-law fluid between parallel plates for hydraulic fracturing applications, *Journal of Non-Newtonian Fluid Mechanics* 223 (2015) 141–146. doi:10.1016/j.jnnfm.2015.06.005.
- [35] A. Rodríguez de Castro, G. Radilla, Non-Darcian flow experiments of shear-thinning fluids through rough-walled rock fractures, *Water Resources Research* 52 (2016) 9020–9035. doi:10.1002/2016WR019406.
- [36] A. Rodríguez de Castro, G. Radilla, Flow of yield stress and Carreau fluids through rough-walled rock fractures: Prediction and experiments, *Water Resources Research* 53 (7) (2017) 6197–6217. doi:10.1002/2017WR020520.
- [37] R. Zimmerman, S. Kumar, G. Bodvarsson, Lubrification theory analysis of the permeability of rough-walled fractures, *International Journal of Rock Mechanics and Mining Sciences & Geomechanics Abstracts* 28(4) (1991) 325–331. doi:10.1016/0148-9062(91)90597-F.
- [38] T. Q. Nguyen, H.-H. Kausch, Mechanochemical degradation in transient elongational flow, in: *Macromolecules: Synthesis, Order and Advanced Properties*, Springer, 1992, pp. 73–182.